

MAIC-2, a latitudinal model for the Martian surface temperature, atmospheric water transport and surface glaciation

RALF GREVE*

Institute of Low Temperature Science, Hokkaido University,
Kita-19, Nishi-8, Kita-ku, Sapporo 060-0819, Japan

BJÖRN GRIEGER

European Space Astronomy Centre, P.O. Box – Apdo. de Correos 78,
28691 Villanueva de la Cañada, Madrid, Spain

OLIVER J. STENZEL

Max Planck Institute for Solar System Research,
Max-Planck-Straße 2, 37191 Katlenburg-Lindau, Germany

Abstract

The Mars Atmosphere-Ice Coupler MAIC-2 is a simple, latitudinal model, which consists of a set of parameterizations for the surface temperature, the atmospheric water transport and the surface mass balance (condensation minus evaporation) of water ice. It is driven directly by the orbital parameters obliquity, eccentricity and solar longitude (L_s) of perihelion. Surface temperature is described by the Local Insolation Temperature (LIT) scheme, which uses a daily and latitude-dependent radiation balance, includes a treatment of the seasonal CO₂ cap, and has been validated against the surface temperatures from the Mars Climate Database. The evaporation rate of water is calculated by an expression for free convection, driven by density differences between water vapor and ambient air, and the condensation rate follows from the assumption that any water vapour which exceeds the local saturation pressure condenses instantly. Atmospheric transport of water vapour is assumed to be purely diffusive, with an adjustable diffusion coefficient. For a static water-ice-cap model (glacial flow neglected), the evolution of the ice thickness is simply governed by the difference between condensation and evaporation. Simulations with fixed orbital parameters show that low obliquities favour deposition of ice in high latitudes and vice versa. A transient scenario driven by a computed history of orbital parameters over the last 5 million years produces very mobile ice, including “ice ages” at high obliquity during which the ice cover extends to the lower latitudes.

*E-mail: greve@lowtem.hokudai.ac.jp

1 Introduction

On time scales of 10^5 – 10^6 years, Mars has experienced large periodic changes of the orbital elements obliquity, eccentricity and equinox precession. These changes have an impact on the Martian climate. The obliquity determines the strength of the seasons and the latitudinal distribution of mean solar insolation. The eccentricity determines the magnitude of the asymmetry of insolation with season, and the equinox precession determines the timing of the asymmetry of solar insolation with season. On Earth, the so-called Milankovitch cycles of much weaker orbital changes with periods of 20, 40 and 100 ka are considered driving forces for climate variations like the glacial/interglacial cycles. It can, therefore, be expected that the main Martian $\pm 10^\circ$ obliquity cycles with periods of 125 ka and 1.3 Ma and the secular shift from high to low average obliquities at 4–5 Ma ago (Laskar et al. 2004, shown in Fig. 1) have significant impacts on the climate and the polar layered deposits (PLDs) due to large insolation changes in the polar regions.

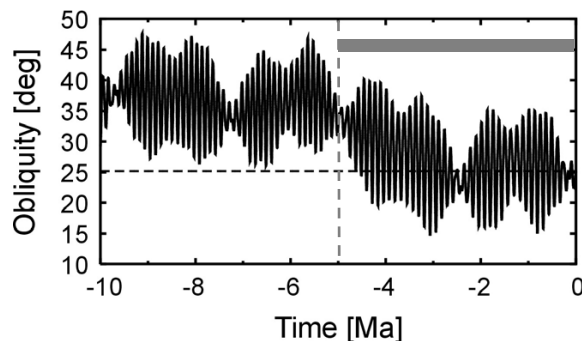


Figure 1: Martian obliquity for the last 10 Ma (Laskar et al. 2004). The grey bar indicates the most recent 5-Ma period with relatively low average obliquity, which favours the formation of polar deposits.

This idea is supported by the presence of light-dark layers in the PLDs, which are exposed in the surface troughs and close to the margins, and which are actually the reason for the term “polar *layered* deposits”. These layers indicate a strongly varying dust content of the ice due to varying climatic conditions in the past. During periods of high obliquities, insolation in the polar regions is large, which entails higher sublimation rates of superficial ice of the PLDs and probably of permafrost in the ground. This may lead to the formation of a thicker and dustier atmosphere, so that dust accumulates on the PLDs. By contrast, during periods of low obliquities, the atmosphere is thin and dust deposition is low, so that clean ice forms at the surface of the PLDs. Along this line of reasoning, Head et al. (2003) presented evidence for past glaciation in the mid-latitudes and suggested that Mars experienced “ice ages” during periods of high obliquity like that from about 2.1 to 0.4 Ma ago (with obliquity maxima of $\approx 35^\circ$). These ice ages were supposedly characterized by warmer polar climates, enhanced mass loss of the PLDs due to sublimation and the formation of meters-thick ice deposits equatorward to approximately 30°N/S .

In a number of studies, General Circulation Models (GCMs) have been applied to the Martian atmosphere (e.g., Pollack et al. 1990, Read et al. 1997, Forget et al. 1999, Richardson and Wilson 2002, Haberle et al. 2003, Takahashi et al. 2003). These models,

all derivatives of Earth GCMs, solve the equations of fluid dynamics and thermodynamics and include e.g. the processes of radiative transfer, cloud formation, regolith-atmosphere water exchange, and advective transport of dust and trace gases. However, they have essentially been designed to simulate the present-day atmosphere in as much detail as possible, and thus are computationally too expensive to permit long-term paleoclimate studies. Segschneider et al. (2005) and Stenzel et al. (2007) adapted an Earth System Model of Intermediate Complexity (EMIC) to Mars. This “Planet Simulator Mars” (PlaSim-Mars, formerly called “Mars Climate Simulator”) allows in principle simulations over longer, climatological time scales. So far, only scenarios for present-day conditions and varied obliquity angles have been considered, and the impact on the PLDs has been studied by coupling PlaSim-Mars with the three-dimensional, dynamic/thermodynamic ice-sheet model SICOPOLIS (<http://sicopolis.greveweb.net/>). In addition to that, simple one-dimensional models have been used to study specific processes that do not require full solution of the dynamic equations. Examples are the radiative transfer model by Gierasch and Goody (1968), the energy balance model by Armstrong et al. (2004), regolith-atmosphere water exchange (Jakosky 1985), and formation of water ice clouds (Michelangeli et al. 1993).

In this study we aim at simulating the surface glaciation of the entire planet with a simple model that depends only on latitude and time. This model, termed the Mars Atmosphere-Ice Coupler Version 2, or MAIC-2 in short, consists of a set of parameterizations for the surface temperature, the atmospheric water transport and the surface mass balance (condensation minus evaporation) of water ice. It is driven directly by the orbital parameters obliquity, eccentricity and solar longitude (L_s) of perihelion, which were published by Laskar et al. (2004) for the period from 20 million years ago until 10 million years into the future. MAIC-2 is applied to two different kinds of scenarios, namely (i) scenarios with orbital parameters kept fixed over time, and (ii) a transient scenario forced by the history of orbital parameters over the last 5 million years. The evolution of surface glaciation is studied for these scenarios under the simplifying assumption of negligible glacial flow, so that changes of local ice thickness are exclusively determined by the local surface mass balance provided by MAIC-2.

2 Model MAIC-2

2.1 Timekeeping and orbital position

We use the timekeeping of PlaSim-Mars (see Sect. 1), in which a Martian year consists of 12 months of 56 days (sols) length. A day has 24 hours of 61.5 minutes length, and a minute is 60 SI seconds long.

In order to compute the relationship between solar longitude L_s and time t , let us identify the beginning of a Martian year with the northern hemisphere vernal equinox ($L_s = 0^\circ$). The orbit of Mars around the sun is described by the ellipse

$$r(\psi) = \frac{p}{1 + \varepsilon \cos \psi}, \quad (1)$$

where r is the distance Sun – Mars, ψ the orbital position measured from the perihelion (“true anomaly”), p the semi-latus rectum and ε the eccentricity. By combining this

equation and the conservation of angular momentum l ,

$$l = mr^2\dot{\psi} \quad (2)$$

(where m denotes the mass of Mars), we find

$$\dot{\psi} = \frac{l}{mr^2} = \frac{l}{mp^2} (1 + \varepsilon \cos \psi)^2 = \Omega (1 + \varepsilon \cos \psi)^2 \quad \left(\Omega := \frac{l}{mp^2} \right). \quad (3)$$

Let $L_{s,p}$ be the solar longitude of perihelion, then

$$\psi = L_s - L_{s,p}, \quad (4)$$

and since $L_{s,p}$ varies only slowly over time, we can rewrite Eq. (3) as

$$\dot{L}_s = \Omega [1 + \varepsilon \cos(L_s - L_{s,p})]^2. \quad (5)$$

This equation can be integrated numerically over a full Martian year (from vernal equinox to vernal equinox) for any values of ε and $L_{s,p}$ by a simple Euler-forward scheme. The initial condition is $L_s = 0^\circ$, and the parameter Ω is adjusted iteratively such that after one Martian year the orbit is closed ($L_s = 360^\circ$), starting from the initial guess $\Omega_{\text{init}} = 2\pi/(1 \text{ Martian year})$ [which is the correct value for a circular orbit with $\varepsilon = 0$].

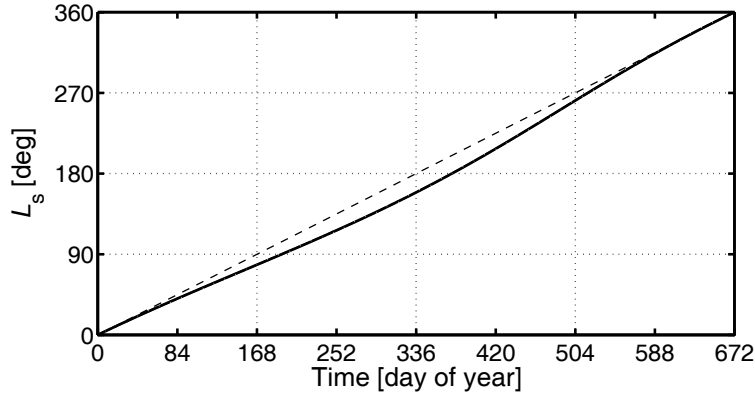


Figure 2: Relationship between solar longitude L_s and time t for present-day conditions (solid line). For comparison, the dashed line shows the linear relationship for a circular orbit.

For present-day conditions ($\varepsilon = 0.093$, $L_{s,p} = 251.0^\circ$), the result is shown in Fig. 2. Since the eccentricity is much larger for Mars than for Earth, the relationship between L_s and t is significantly different from a linear one. The deviation becomes as large as 21° ($L_s = 158.97^\circ$ instead of 180° for day of year 336, leading to a lag of the northern autumnal equinox by 37.7 Martian days).

2.2 Surface pressure

The seasonal variation of surface pressure P is neglected, and we use a global annual mean value ($P = 700 \text{ Pa}$) instead.

2.3 Surface temperature

In order to derive a parameterization for the daily mean local surface temperature $T(\phi, t)$ (depending on latitude ϕ and time t), we start with the radiation balance

$$\sigma T^4 = (1 - A) F, \quad (6)$$

where σ is the Stefan-Boltzmann constant ($\sigma = 5.67 \times 10^{-8} \text{ W m}^{-2} \text{ K}^{-4}$), A is the surface albedo (globally $A = 0.3$ assumed) and F is the local daily mean insolation as a function of the orbital parameters obliquity, eccentricity and solar longitude of perihelion (Laskar et al. 2004). In the absence of seasonal CO_2 frost, Eq. (6) provides reasonable results for the surface temperature. However, the equation does not account for the fact that at

$$T = T_{\text{cond}} = \frac{b}{a - \ln P [\text{hPa}]} \quad (7)$$

(where P is the surface pressure, $a = 23.3494$ and $b = 3182.48 \text{ K}$; James et al. 1992) condensation of the atmospheric CO_2 (formation of the seasonal ice cap) sets in. For $P = 700 \text{ Pa}$, Eq. (7) yields a value of $T_{\text{cond}} = 148.7 \text{ K}$. Since the atmosphere never freezes out completely, this value constitutes the minimum of surface temperatures which can be realized.

In order to find out when the seasonal CO_2 ice cap at a given latitude ϕ is present, and therefore $T = T_{\text{cond}}$ holds, the seasonal cap is assumed to exist between the onset of the polar night (t_{dusk}) and an unknown time t after the end of the polar night (t_{dawn}). During the polar night, condensation takes place, and the amount of formed CO_2 frost corresponds to the energy (per area unit)

$$W_{\text{cond}} = \int_{t_{\text{dusk}}}^{t_{\text{dawn}}} \sigma T_{\text{cond}}^4 dt. \quad (8)$$

After dawn, the solar insolation causes the CO_2 frost to evaporate, which requires the energy

$$W_{\text{evap}} = \int_{t_{\text{dawn}}}^t \left((1 - A_{\text{CO}_2}) F - \sigma T_{\text{cond}}^4 \right) dt, \quad (9)$$

where $A_{\text{CO}_2} = 0.6$ is the albedo of the CO_2 frost. The time t at which the CO_2 frost has evaporated completely follows from

$$W_{\text{evap}} = W_{\text{cond}}. \quad (10)$$

The scheme defined by the radiation balance (6), modified by CO_2 condensation following Eqs. (8)–(10), is referred to as *Local Insolation Temperature scheme* (LIT); it was first laid down by B. Grieger (2004; talk at 2nd MATSUP workshop, Darmstadt, Germany). The resulting daily mean surface temperatures over one Martian year for present-day conditions are shown in Fig. 3. They agree well with the data given in the Mars Climate Database (Lewis et al. 1999). A problem is, though, that the scheme does not reproduce the observed year-round CO_2 ice cover of the south pole.

The Mars Atmosphere-Ice Coupler with the LIT scheme (with the simplifying assumption $A = A_{\text{CO}_2} = 0.3$) and the simple treatment of the surface mass balance described by Greve et al. (2004) and Greve and Mahajan (2005) is referred to as “MAIC-1.5”. It was used by these authors to drive simulations of the north polar layered deposits with the ice-sheet model SICOPOLIS.

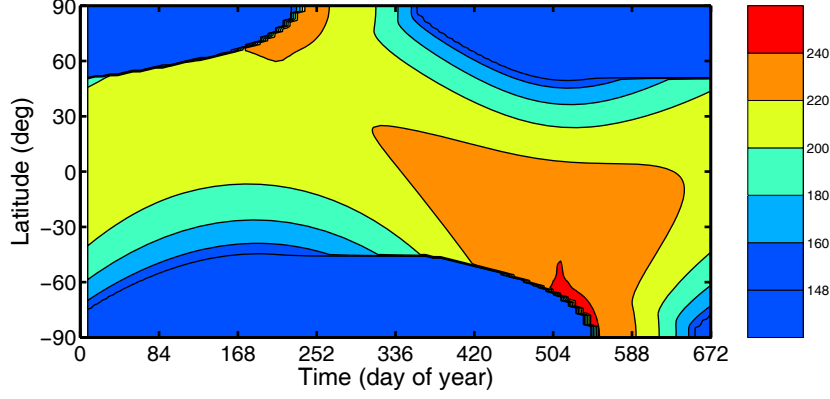


Figure 3: Daily mean surface temperature (in K) of the LIT scheme for present-day conditions.

2.4 Saturation pressure of water vapour

The water-vapour saturation pressure P_{sat} is obtained from the Clausius-Clapeyron relation, which can be integrated only approximately. Different approximations are available; we use the Magnus-Teten formula for water vapour over ice (Murray 1967)

$$P_{\text{sat}}(T) = A \exp \left(\frac{B(T - T_0)}{T - C} \right), \quad (11)$$

with $A = 610.66 \text{ Pa}$, $B = 21.875$, $C = 7.65 \text{ K}$ and $T_0 = 273.16 \text{ K}$, which has also been implemented in the Planet Simulator Mars (Stenzel et al. 2007).

2.5 Evaporation

Ingersoll (1970) discussed the water vapour mass flux in the Martian carbon dioxide atmosphere. The evaporation rate E of water from the surface, expressed as a mass flux in $\text{kg m}^{-2} \text{ s}^{-1}$, is

$$E = E_0 \times 0.17 \Delta\eta \rho D \left(\frac{(\Delta\rho/\rho) g}{\nu^2} \right)^{1/3}, \quad (12)$$

where E_0 is the evaporation factor (default value equal to unity), $\Delta\eta$ the concentration difference at the surface and at distance, ρ the atmospheric density, $\Delta\rho$ the CO_2 density difference at the surface and at distance, D the diffusion coefficient of water in CO_2 , g the acceleration due to gravity and ν the kinematic viscosity of CO_2 (cf. also Sears and Moore 2005). The term $\Delta\eta$ is given by

$$\Delta\eta = \frac{\rho_{\text{w}}^{\text{sat}}}{\rho} = \frac{M_{\text{w}} P_{\text{sat}}}{M_{\text{c}} P}, \quad (13)$$

where $\rho_{\text{w}}^{\text{sat}}$ is the saturation density of water vapour at the surface temperature T and M_{w} and M_{c} are the molecular weights of water and carbon dioxide, respectively. The terms ρ and $\Delta\rho/\rho$ are calculated by applying the ideal gas law,

$$\rho = \frac{M_{\text{c}} P}{RT}, \quad \frac{\Delta\rho}{\rho} = \frac{(M_{\text{c}} - M_{\text{w}}) P_{\text{sat}}}{M_{\text{c}} P - (M_{\text{c}} - M_{\text{w}}) P_{\text{sat}}}, \quad (14)$$

Quantity	Value
Gravity acceleration, g	3.72 m s^{-2}
Diffusion coefficient, D	$1.4 \times 10^{-3} \text{ m}^2 \text{ s}^{-1}$
Kinematic viscosity of CO_2 , ν	$6.93 \times 10^{-4} \text{ m}^2 \text{ s}^{-1}$
Universal gas constant, R	$8.314 \text{ J mol}^{-1} \text{ K}^{-1}$
Molar mass of water, M_w	$1.802 \times 10^{-2} \text{ kg mol}^{-1}$
Molar mass of CO_2 , M_c	$4.401 \times 10^{-2} \text{ kg mol}^{-1}$

Table 1: Physical parameters for the evaporation model of MAIC-2.

where R is the universal gas constant. Parameter values are given in Table 1.

Sears and Moore (2005) state that a $10\text{--}15 \text{ m s}^{-1}$ wind increases evaporation rates by about a factor 10, and that the evaporation rate of ice is probably about half that of liquid water. Such effects can be accounted for by setting the evaporation factor in Eq. (12) to a value different from unity. The dependence of evaporation on surface temperature and pressure for $E_0 = 1$ is illustrated in Fig. 4.

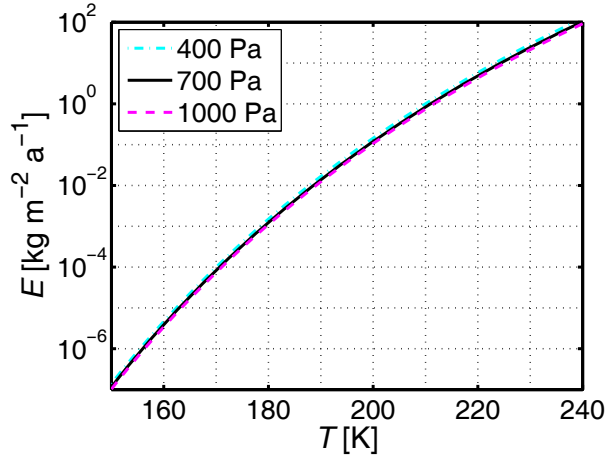


Figure 4: Dependence of the evaporation rate E on the surface temperature T for surface pressures $P = 400, 700$ and 1000 Pa , and $E_0 = 1$.

The above equation (12) is valid for an ice cap in contact with the atmosphere. By contrast, for the case of ground ice, we assume that the evaporation rate is reduced with increasing thickness H_{reg} of the ice-free regolith layer (which separates the atmosphere from the ground ice),

$$E \rightarrow E \times \exp\left(-\frac{H_{\text{reg}}}{\gamma_{\text{reg}}}\right), \quad (15)$$

where γ_{reg} is the regolith-insulation coefficient, chosen as $\gamma_{\text{reg}} = 0.1 \text{ m}$.

2.6 Condensation

The water content ω in the atmosphere is expressed as area mass density, i. e. in units of kg m^{-2} . Multiplied with the gravity acceleration g , this becomes equivalent to the partial

pressure of water vapour at the surface. Thus we compare this pressure to the water vapor saturation pressure P_{sat} and condense all excessive water, i. e.

$$C = \frac{1}{\Delta t} \left(\omega - \frac{P_{\text{sat}}(T)}{g} \right), \quad \text{if } g\omega > P_{\text{sat}}(T), \quad (16)$$

where Δt is the model time step. Note that this is a very simplistic approach because in reality condensation takes place higher in the atmosphere where the temperature may differ considerably from the surface temperature.

2.7 Transport

The water content ω in the atmosphere is expressed as area mass density. As evaporation E (cf. Sect. 2.5) and condensation C (cf. Sect. 2.6) are expressed as mass fluxes in units of $\text{kg m}^{-2} \text{s}^{-1}$, it is simply

$$\frac{\partial \omega}{\partial t} = -\nabla \cdot \mathbf{F} + E - C, \quad (17)$$

with \mathbf{F} being the (horizontal) water transport in units of $\text{kg m}^{-1} \text{s}^{-1}$. The water transport is assumed to be purely diffusive, thus

$$\mathbf{F} = -K \nabla \omega, \quad (18)$$

where K is the adjustable diffusion coefficient in units of $\text{m}^2 \text{s}^{-1}$. Inserting Eq. (18) in Eq. (17) yields

$$\frac{\partial \omega}{\partial t} = K \nabla^2 \omega + E - C. \quad (19)$$

We assume for simplicity that the water content ω only depends on latitude ϕ and time t , but not on longitude λ . Thus, it can be expressed as a function $\omega = \omega(\phi, t)$. With the Laplacian for spherical coordinates, Eq. (19) yields

$$\frac{\partial \omega}{\partial t} = \frac{K}{R^2 \cos \phi} \frac{\partial}{\partial \phi} \left(\cos \phi \frac{\partial \omega}{\partial \phi} \right) + E - C, \quad (20)$$

where R denotes the radius of the planet ($R = 3396 \text{ km}$). Note that instantaneous mixing of water vapour in the atmosphere can formally be obtained as the limit of infinite diffusivity, $K \rightarrow \infty$.

The MAIC version with the LIT scheme of Sect. 2.3 and the surface mass balance of water ice that results from Sects. 2.5–2.7 is referred to as “MAIC-2”.

2.8 Ice evolution

With the condensation C and the evaporation E , the net mass balance a_{net} of the ice caps, expressed in $\text{m ice equiv. s}^{-1}$, is

$$a_{\text{net}} = \frac{C - E}{\rho_{\text{ice}}}, \quad (21)$$

where $\rho_{\text{ice}} = 910 \text{ kg m}^{-3}$ is the density of ice. For a static model (glacial flow neglected), the evolution of the ice thickness, H , is then simply

$$\frac{\partial H}{\partial t} = a_{\text{net}}. \quad (22)$$

Note that we allow for negative ice thicknesses ($H < 0$). Such a situation is interpreted as ground ice under an ice-free regolith layer of thickness $H_{\text{reg}} = |H|$.

The validity of the assumption of negligible glacial flow is debatable. On the one hand, modelled ice flow speeds on Mars are generally slow, even during periods of high obliquity (Greve et al. 2004, Greve and Mahajan 2005). On the other hand, locally enhanced glacial flow may occur near chasmata and troughs of the PLDs (Hvidberg 2003, Greve 2008), and Winebrenner et al. (2008) argue that the overall topography of Gemina Lingula (also known as Titania Lobe), the lobe of the northern PLDs to the south of Chasma Boreale, was likely shaped by past glacial flow. In this study, we will stick to the simple, static ice model, but consider the inclusion of glacial flow for future work.

3 Simulations

We will now discuss the application of MAIC-2 to four different scenarios. Three of them are of “academic” nature with orbital parameters kept fixed over time, whereas the fourth one employs a realistic, time-dependent forcing over the last 5 million years. In order to carry out these simulations, a finite-difference/finite-volume discretization of the model equations of MAIC-2 has been derived (see Appendix A for details) and coded in the Fortran program `maic2.F90`. The parameter E_0 in the evaporation scheme [Eq. (12)] is set to unity (thus increased evaporation due to wind is neglected), instantaneous mixing of water vapour in the atmosphere is assumed (diffusivity $K \rightarrow \infty$), and an equidistant grid spacing of $\Delta\phi = 1^\circ$ was chosen (the formulation in Appendix A allows also for non-equidistant spacings).

3.1 Fixed orbital parameters

The set-up of *simulation #1* is as follows:

- Present-day orbital parameters kept fixed:
 - Obliquity $\phi = 25.2^\circ$.
 - Eccentricity $\varepsilon = 0.093$.
 - Solar longitude of perihelion $L_{\text{s,p}} = 251.0^\circ$.
- Initial ice layer of 20 m thickness on the entire surface of Mars.
- Simulation time 10^7 Martian years, time-step $1/84$ Martian years ($= 8$ sols).

The resulting net mass balance of water ice in the first Martian year of the simulation is shown in Fig. 5. The distribution resembles that of the surface temperature (Fig. 3). The seasonal CO_2 caps are efficient cold traps for atmospheric water vapour, which leads to strongly positive mass balances in the Martian polar regions for most of the year. By contrast, in the lower latitudes negative mass balances prevail, so that the initial ice layer of constant thickness is redistributed towards the poles.

The evolution of the ice thickness for the entire simulation time of 10^7 Martian years is depicted in Fig. 6. It is striking that the redistribution of ice towards the poles is strongly

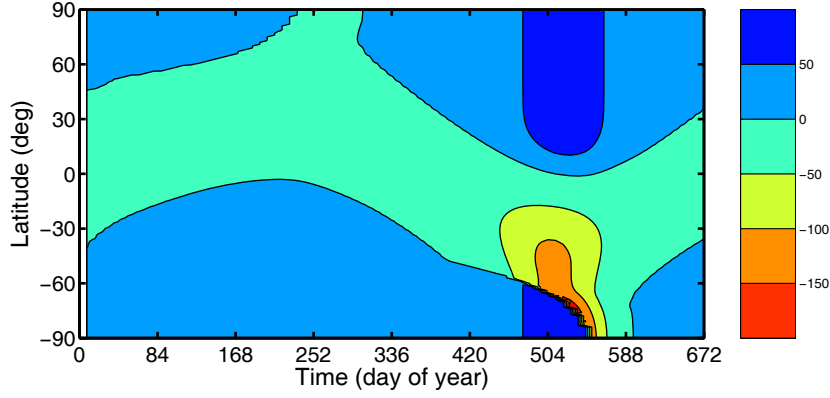


Figure 5: Simulation #1: Net surface mass balance (in mm ice equiv. a⁻¹) in the first Martian year.

antisymmetric. At 10^3 and 10^4 Martian years, MAIC-2 produces more pronounced ice deposits in the northern hemisphere and less pronounced ones in the southern hemisphere. At 10^5 Martian years and later, the ice migrates entirely to the northern hemisphere and concentrates around the north pole. In fact, the simulated north polar deposits at 10^7 Martian years resemble the currently existing PLDs in extent and thickness (see below, right panel of Fig. 10), while the simulated south polar region is ice-free.

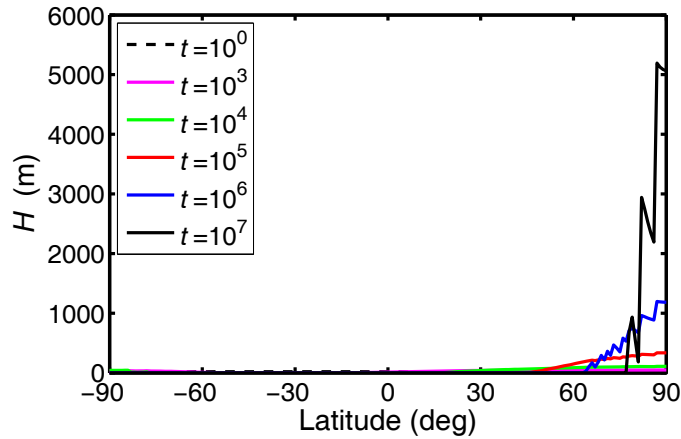


Figure 6: Simulation #1: Evolution of the ice thickness H (time t in Martian years).

The reason for this behaviour is the hemispheric asymmetry of the daily mean surface temperature (Fig. 3). As a consequence of the closer proximity of Mars to the Sun during southern summer, the southern summer is distinctly warmer than the northern summer. This leads to large evaporation rates during southern summer and thus a large amount of water vapour in the atmosphere, which is trapped preferably in the winter-cold high northern latitudes. Conversely, the northern summer is less warm, evaporation rates are lower, and therefore the potential for water ice accumulation in the south polar region is much smaller.

A numerical instability is visible in Fig. 6 for the ice-thickness distributions at 10^6 and 10^7 Martian years, which appear slightly jagged. This is probably related to the neglect of glacial flow, which would otherwise smooth the ice surface out efficiently.

Simulation #2 has been run with essentially the same set-up as simulation #1; however, the obliquity has been reduced to $\phi = 15^\circ$. This is approximately equal to the minimum value which occurred during the last 4 Ma (Fig. 1). The resulting evolution of the ice thickness is shown in Fig. 7. As a result of the weaker seasonal cycle due to the lower obliquity, the hemispheric asymmetry is less pronounced than for simulation #1. Consequently, the ice deposits are now bipolar and almost symmetric between the north and south polar regions. Compared to the real PLDs, the simulated polar deposits after 10^7 Martian years are thinner and wider (extent to $\sim 70^\circ\text{N/S}$).

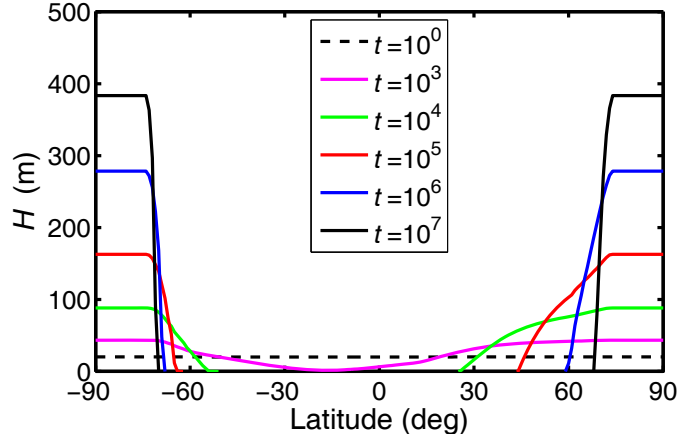


Figure 7: Simulation #2: Evolution of the ice thickness H (time t in Martian years).

For *simulation #3*, the obliquity has been changed to $\phi = 35^\circ$, which is approximately equal to the maximum value during the last 4 Ma. This makes the seasons more extreme. Figure 8 displays the resulting evolution of the ice thickness. Like in simulation #1, the ice is preferentially deposited in the northern hemisphere due to the warmer southern summers. However, now the poles receive substantial insolation during the respective summer season, so that the northern hemispheric ice deposits are not thickest at the north pole any more. Instead, ice deposition is favoured in the mid-latitudes, and beyond 10^4 Martian years simulation time the deposits develop a thickness maximum as far south as $\sim 25^\circ\text{N}$.

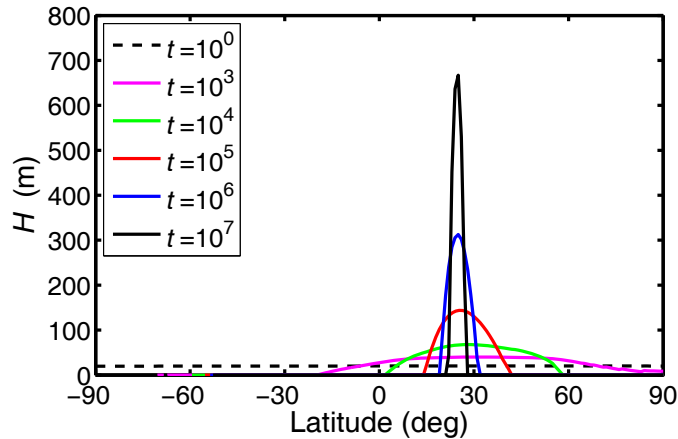


Figure 8: Simulation #3: Evolution of the ice thickness H (time t in Martian years).

3.2 Evolution over the last five million years

Simulation #4 attempts at providing a realistic, time-dependent scenario over the last 5 million years. The set-up is as follows:

- History of orbital parameters by Laskar et al. (2004).
- Simulation time from 5×10^6 years ago until today (Fig. 1), time-step 0.02 years.
- Initial ice layer of 20 m thickness on the entire surface.

The simulated maximum ice thickness and its position on the planet are shown in Fig. 9. The simulation produces a very mobile glaciation, the maximum thickness being less than 300 m for most of the time. Only during the periods around 2.5 Ma ago and the present when the amplitude of the main obliquity cycle of 125 ka was small, larger thicknesses of up to 800 m occur. The position where the maximum thickness occurs flip-flops between the poles for most of the time, but it can also occur in lower latitudes and even close to the equator.

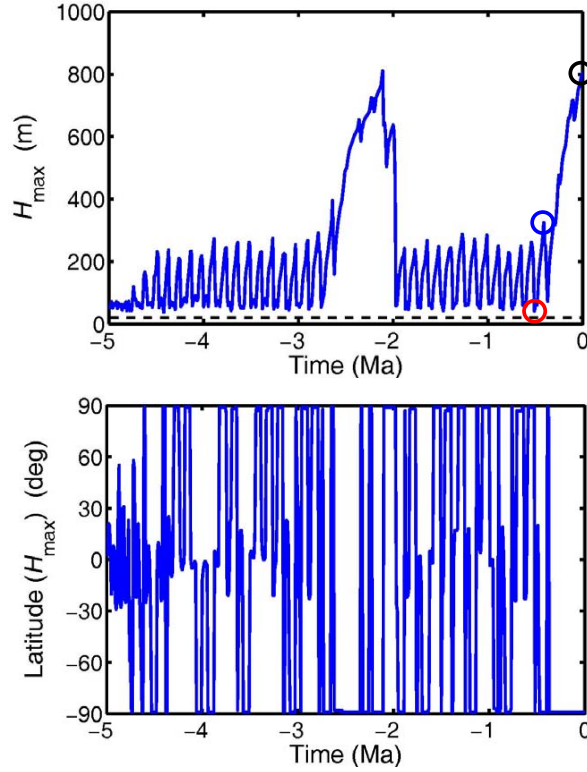


Figure 9: Simulation #4: [Top] Maximum ice thickness (the circle marks correspond to the time slices shown in Fig. 10). [Bottom] Latitude of maximum ice thickness.

In order to illustrate this behaviour in more detail, Fig. 10 depicts the distribution of the simulated ice thickness for three selected time slices. The first time slice, 0.51 Ma ago, is characterized by a high obliquity (33.8°), a low maximum ice thickness (41.8 m) which occurs in the low southern latitudes (at 24°S) and a glaciation which covers the entire mid and low latitudes on both hemispheres. The second time slice, 0.41 Ma ago,

at an intermediate obliquity of 27.6° following a minimum of 19.5° which occurred 44 ka earlier, shows bipolar ice deposits with a rather high maximum ice thickness of 325 m at the south pole. The third time slice is the present, with an obliquity of 25.2° following a ~ 0.3 Ma period with only small changes (within less than 5°). For the present, simulation #4 predicts bipolar ice deposits with a maximum thickness of 804 m at the south pole, while at the north pole the ice thickness reaches 688 m. Both polar deposits stretch equatorward to approximately 70°N/S , similar to those of simulation #2. The simulated polar ice deposits are therefore about three times thinner and cover about three times larger areas than the real ones (also shown in Fig. 10), but the gross picture of two polar deposits centered around the poles is reproduced well by the simulation.

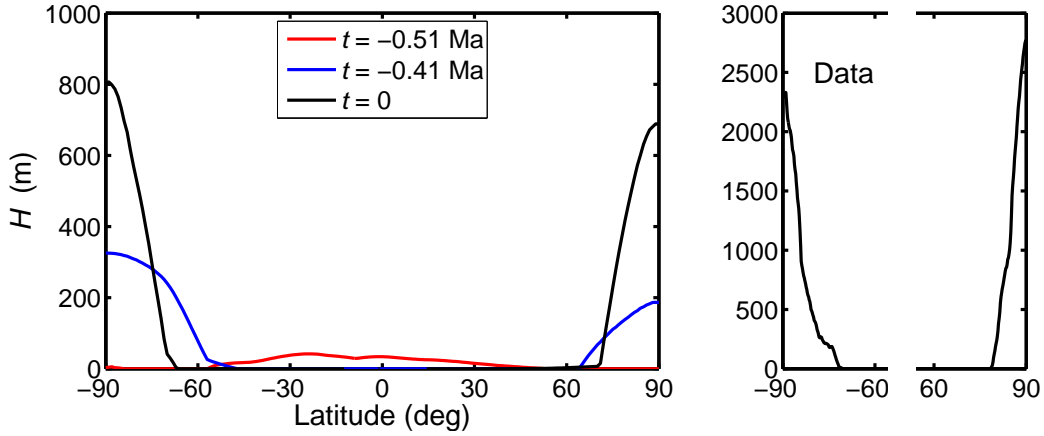


Figure 10: [Left] Simulation #4: Ice thickness H for three selected time slices (which correspond to the marks in the top panel of Fig. 9.) [Right] Observational data of the ice thickness of the present-day PLDs. They have been obtained by subtracting the MOLA surface topography (Zuber et al. 1998, Smith et al. 1999) from the basal topography computed by a smooth extrapolation of the ice-free ground (Greve et al. 2004) and subsequent zonal averaging. Note the different scales of the two panels.

4 Discussion and conclusion

The simulations with fixed orbital parameters presented in Sect. 3.1 confirm the intuitive idea that low obliquities favour deposition of water ice in high latitudes and vice versa. An interesting additional finding is that the polar ice deposits for relatively low obliquities can either occur at one pole only or at both poles, depending on the asymmetry of the seasons in the two hemispheres. The more realistic simulation of Sect. 3.2 with time-dependent orbital forcing produces very mobile ice which is exchanged between the polar regions and the lower latitudes. This exchange is mainly controlled by obliquity, polar deposits being again favoured by low obliquities and lower-latitude deposits by high obliquities. The latter result agrees qualitatively with the findings by Head et al. (2003) who report evidence for “ice ages” on Mars during the period from about 2.1 to 0.4 Ma ago when the obliquity regularly exceeded 30° . According to the authors, the conditions during

this period favoured the deposition of meters-thick, dusty, water-ice-rich material down to latitudes of $\sim 30^\circ$ in both hemispheres.

Some limitations of this study must be noted. Let us recall that the transient simulation of Sect. 3.2 fails to reproduce the present-day, ~ 2.5 -km thick PLDs which are essentially concentrated within 80°N/S . Instead, the simulated present-day deposits are thinner and wider by about a factor of three. A possible explanation for this discrepancy is that the daily cycle of the surface temperature has not been considered so far. Since the amplitude of the daily temperature cycle is zero directly at the poles, but increases rapidly with increasing distance from the poles, it leads (via warm noon-time temperatures) to higher evaporation rates away from the poles. Therefore, inclusion of the daily temperature cycle should produce a stronger concentration of the ice deposits around the poles.

Further, the estimated surface ages of the northern (at most 0.1 Ma) and southern PLDs (about 10 Ma) by Herkenhoff and Plaut (2000), which are based on crater statistics, are consistent with the simulated ice mobility for the north, but not for the south polar region (see Fig. 10). This may be related to the fact that most of the southern PLDs are covered by dust, whereas the water ice of their northern counterpart is exposed to the atmosphere. Consequently, at least for the present-day situation, the northern PLDs can readily exchange water with the atmosphere, whereas the exchange is blocked to an unknown extent for the southern PLDs. This problem requires further attention.

Acknowledgements

This work was partly carried out within the project “Evolution and dynamics of the Martian polar ice caps over climatic cycles” supported by the Research Fund of the Institute of Low Temperature Science, Sapporo, Japan.

References

- Armstrong, J. C., C. B. Leovy and T. Quinn. 2004. A 1 Gyr climate model for Mars: new orbital statistics and the importance of seasonally resolved polar processes. *Icarus*, **171** (2), 255–271. doi:10.1016/j.icarus.2004.05.007.
- Forget, F., F. Hourdin, R. Fournier, C. Hourdin, O. Talagrand, M. Collins, S. R. Lewis, P. L. Read and J.-P. Huot. 1999. Improved general circulation models of the Martian atmosphere from the surface to above 80 km. *J. Geophys. Res.*, **104** (E10), 24155–24175.
- Gierasch, P. and R. Goody. 1968. A study of the thermal and dynamical structure of the martian lower atmosphere. *Planet. Space Sci.*, **16** (5), 615–646.
- Greve, R. 2008. Scenarios for the formation of Chasma Boreale, Mars. *Icarus*, **196** (2), 359–367. doi:10.1016/j.icarus.2007.10.020.
- Greve, R. and R. A. Mahajan. 2005. Influence of ice rheology and dust content on the dynamics of the north-polar cap of Mars. *Icarus*, **174** (2), 475–485. doi:10.1016/j.icarus.2004.07.031.
- Greve, R., R. A. Mahajan, J. Segschneider and B. Grieger. 2004. Evolution of the north-polar cap of Mars: a modelling study. *Planet. Space Sci.*, **52** (9), 775–787. doi:10.1016/j.pss.2004.03.007.

- Haberle, R. M., J. R. Murphy and J. Schaeffer. 2003. Orbital change experiments with a Mars general circulation model. *Icarus*, **161** (1), 66–89.
- Head, J. W., J. F. Mustard, M. A. Kreslavsky, R. E. Milliken and D. R. Marchant. 2003. Recent ice ages on Mars. *Nature*, **426** (6968), 797–802. doi:10.1038/nature02114.
- Herkenhoff, K. E. and J. J. Plaut. 2000. Surface ages and resurfacing rates of the polar layered deposits on Mars. *Icarus*, **144** (2), 243–253.
- Hvidberg, C. S. 2003. Relationship between topography and flow in the north polar cap on Mars. *Ann. Glaciol.*, **37**, 363–369.
- Ingersoll, A. P. 1970. Mars: Occurrence of liquid water. *Science*, **168** (3934), 972–973.
- Jakosky, B. M. 1985. The seasonal cycle of water on Mars. *Space Sci. Rev.*, **41**, 131–200.
- James, P. B., H. H. Kieffer and D. A. Paige. 1992. The seasonal cycle of carbon dioxide on Mars. In: H. H. Kieffer, B. M. Jakosky, C. W. Snyder and M. S. Matthews (Eds.), *Mars*, pp. 934–968. University of Arizona Press, Tucson.
- Laskar, J., A. C. M. Correia, M. Gastineau, F. Joutel, B. Levrard and P. Robutel. 2004. Long term evolution and chaotic diffusion of the insolation quantities of Mars. *Icarus*, **170** (2), 343–364. doi:10.1016/j.icarus.2004.04.005.
- Lewis, S. R., M. Collins, P. L. Read, F. Forget, F. Hourdin, R. Fournier, C. Hourdin, O. Talagrand and J.-P. Huot. 1999. A climate database for Mars. *J. Geophys. Res.*, **104** (E10), 24177–24194.
- Michelangeli, D. V., O. B. Toon, R. M. Haberle and J. B. Pollack. 1993. Numerical simulations of the formation and evolution of water ice clouds in the Martian atmosphere. *Icarus*, **102** (2), 261–285.
- Murray, F. W. 1967. On the computation of saturation vapor pressure. *J. Appl. Meteorol.*, **6**, 203–204.
- Pollack, J. B., R. M. Haberle, J. Schaeffer and H. Lee. 1990. Simulation of the general circulation of the Martian atmosphere 1. Polar processes. *J. Geophys. Res.*, **95** (B2), 1447–1473.
- Read, P. L., M. Collins, F. Forget, R. Fournier, F. Hourdin, S. R. Lewis, O. Talagrand, F. W. Taylor and N. P. J. Thomas. 1997. A GCM climate database for Mars: for mission planning and for scientific studies. *Adv. Space Res.*, **19**, 1213–1222.
- Richardson, M. I. and R. J. Wilson. 2002. A topographically forced asymmetry in the martian circulation and climate. *Nature*, **416** (6878), 298–301. doi:10.1038/416298a.
- Sears, D. W. G. and S. R. Moore. 2005. On laboratory simulation and the evaporation rate of water on Mars. *Geophys. Res. Lett.*, **32** (16), L16202. doi:10.1029/2005GL023443.
- Segschneider, J., B. Grieger, H. U. Keller, F. Lunkeit, E. Kirk, K. Fraedrich, A. Rodin and R. Greve. 2005. Response of the intermediate complexity Mars Climate Simulator to different obliquity angles. *Planet. Space Sci.*, **53** (6), 659–670. doi:10.1016/j.pss.2004.10.003.

- Smith, D. E., M. T. Zuber, S. C. Solomon, R. J. Phillips, J. W. Head, J. B. Garvin, W. B. Banerdt, D. O. Muhleman, G. H. Pettengill, G. A. Neumann, F. G. Lemoine, J. B. Abshire, O. Aharonson, C. D. Brown, S. A. Hauck, A. B. Ivanov, P. J. McGovern, H. J. Zwally and T. C. Duxbury. 1999. The global topography of Mars and implications for surface evolution. *Science*, **284** (5419), 1495–1503.
- Stenzel, O. J., B. Grieger, H. U. Keller, R. Greve, K. Fraedrich, E. Kirk and F. Lunkeit. 2007. Coupling Planet Simulator Mars, a general circulation model of the Martian atmosphere, to the ice sheet model SICOPOLIS. *Planet. Space Sci.*, **55** (14), 2087–2096. doi:10.1016/j.pss.2007.09.001.
- Takahashi, Y. O., H. Fujiwara, H. Fukunishi, M. Odaka, Y.-Y. Hayashi and S. Wanabe. 2003. Topographically induced north-south asymmetry of the meridional circulation in the Martian atmosphere. *J. Geophys. Res.*, **108** (E3), 5018. doi:10.1029/2001JE001638.
- Winebrenner, D. P., M. R. Koutnik, E. D. Waddington, A. V. Pathare, B. C. Murray, S. Byrne and J. L. Bamber. 2008. Evidence for ice flow prior to trough formation in the martian north polar layered deposits. *Icarus*, **195** (1), 90–105. doi:10.1016/j.icarus.2007.11.030.
- Zuber, M. T., D. E. Smith, S. C. Solomon, J. B. Abshire, R. S. Afzal, O. Aharonson, K. Fishbaugh, P. G. Ford, H. V. Frey, J. B. Garvin, J. W. Head, A. B. Ivanov, C. L. Johnson, D. O. Muhleman, G. A. Neumann, G. H. Pettengill, R. J. Phillips, X. Sun, H. J. Zwally, W. B. Banerdt and T. C. Duxbury. 1998. Observations of the north polar region of Mars from the Mars Orbiter Laser Altimeter. *Science*, **282** (5396), 2053–2060.

A Discrete formulation

A.1 Numerical grid

We envisage a spatially one-dimensional model formulated in dependence on latitude only. The grid points are located at monotonically increasing latitudes

$$\phi_l, \quad l = 0, \dots, L, \quad (23)$$

where $\phi_0 = -\pi/2$ (south pole) and $\phi_L = \pi/2$ (north pole). The generally non-equidistant spacing between subsequent grid points is

$$\Delta\phi_l = \phi_l - \phi_{l-1}, \quad l = 1, \dots, L. \quad (24)$$

Further, we define the latitudes in between grid points (at cell boundaries) as

$$\phi_{l\pm 1/2} = \frac{\phi_l + \phi_{l\pm 1}}{2}. \quad (25)$$

A.2 Diffusive water transport

We derive a finite-volume (FV) discretization of Eq. (20) by integrating it over a latitudinal band between arbitrary boundaries ϕ_a and ϕ_b . With the area element

$$dA = 2\pi R^2 \cos \phi \, d\phi, \quad (26)$$

this yields

$$\begin{aligned}
2\pi R^2 \int_{\phi_a}^{\phi_b} \frac{\partial \omega}{\partial t} \cos \phi \, d\phi &= 2\pi R^2 \int_{\phi_a}^{\phi_b} (E - C) \cos \phi \, d\phi + 2\pi K \int_{\phi_a}^{\phi_b} \frac{\partial}{\partial \phi} \left(\cos \phi \frac{\partial \omega}{\partial \phi} \right) d\phi \\
&= 2\pi R^2 \int_{\phi_a}^{\phi_b} (E - C) \cos \phi \, d\phi \\
&\quad + 2\pi K \left(\cos \phi_b \frac{\partial \omega}{\partial \phi} \Big|_{\phi_b} - \cos \phi_a \frac{\partial \omega}{\partial \phi} \Big|_{\phi_a} \right). \tag{27}
\end{aligned}$$

For any inner point of the model domain, $l = 1, \dots, L-1$, we choose $\phi_a = \phi_{l-1/2}$, $\phi_b = \phi_{l+1/2}$, and approximate the integrals by factoring out $\partial \omega / \partial t$ and $(E - C)$, respectively:

$$\begin{aligned}
\frac{\partial \omega}{\partial t} \Big|_{\phi_l} \int_{\phi_{l-1/2}}^{\phi_{l+1/2}} \cos \phi \, d\phi &= (E_l - C_l) \int_{\phi_{l-1/2}}^{\phi_{l+1/2}} \cos \phi \, d\phi \\
&\quad + \frac{K}{R^2} \left(\cos \phi_{l+1/2} \frac{\partial \omega}{\partial \phi} \Big|_{\phi_{l+1/2}} - \cos \phi_{l-1/2} \frac{\partial \omega}{\partial \phi} \Big|_{\phi_{l-1/2}} \right), \tag{28}
\end{aligned}$$

or

$$\begin{aligned}
\frac{\partial \omega}{\partial t} \Big|_{\phi_l} (\sin \phi_{l+1/2} - \sin \phi_{l-1/2}) &= (E_l - C_l) (\sin \phi_{l+1/2} - \sin \phi_{l-1/2}) \\
&\quad + \frac{K}{R^2} \left(\cos \phi_{l+1/2} \frac{\partial \omega}{\partial \phi} \Big|_{\phi_{l+1/2}} - \cos \phi_{l-1/2} \frac{\partial \omega}{\partial \phi} \Big|_{\phi_{l-1/2}} \right). \tag{29}
\end{aligned}$$

We employ central differences for the spatial derivatives and an Euler forward step for the time derivative. This yields

$$\begin{aligned}
\frac{\omega_l^{n+1} - \omega_l^n}{\Delta t} &= E_l^n - C_l^n + \frac{K}{R^2 (\sin \phi_{l+1/2} - \sin \phi_{l-1/2})} \\
&\quad \times \left(\cos \phi_{l+1/2} \frac{\omega_{l+1}^n - \omega_l^n}{\Delta \phi_{l+1}} - \cos \phi_{l-1/2} \frac{\omega_l^n - \omega_{l-1}^n}{\Delta \phi_l} \right), \tag{30}
\end{aligned}$$

where n is the time index and Δt the time step, so that $t^n = t^0 + n\Delta t$.

For the south pole ($l = 0$), the procedure is slightly different. In this case, we choose $\phi_a = \phi_0 = -\pi/2$, $\phi_b = \phi_{1/2}$, and obtain in analogy to Eq. (29)

$$\begin{aligned}
\frac{\partial \omega}{\partial t} \Big|_{\phi_0} (\sin \phi_{1/2} - \sin \phi_0) &= (E_0 - C_0) (\sin \phi_{1/2} - \sin \phi_0) \\
&\quad + \frac{K}{R^2} \left(\cos \phi_{1/2} \frac{\partial \omega}{\partial \phi} \Big|_{\phi_{1/2}} - \cos \phi_0 \frac{\partial \omega}{\partial \phi} \Big|_{\phi_0} \right). \tag{31}
\end{aligned}$$

With $\cos \phi_0 = 0$, $\sin \phi_0 = -1$ and the same finite differences as above, this yields

$$\frac{\omega_0^{n+1} - \omega_0^n}{\Delta t} = (E_0^n - C_0^n) + \frac{K}{R^2 (1 + \sin \phi_{1/2})} \cos \phi_{1/2} \frac{\omega_1^n - \omega_0^n}{\Delta \phi_1}. \tag{32}$$

Finally, for the north pole ($l = L$), we choose $\phi_a = \phi_{L-1/2}$, $\phi_b = \phi_L = \pi/2$, so that

$$\begin{aligned}
\frac{\partial \omega}{\partial t} \Big|_{\phi_L} (\sin \phi_L - \sin \phi_{L-1/2}) &= (E_L - C_L) (\sin \phi_L - \sin \phi_{L-1/2}) \\
&\quad + \frac{K}{R^2} \left(\cos \phi_L \frac{\partial \omega}{\partial \phi} \Big|_{\phi_L} - \cos \phi_{L-1/2} \frac{\partial \omega}{\partial \phi} \Big|_{\phi_{L-1/2}} \right), \tag{33}
\end{aligned}$$

and with $\cos \phi_L = 0$, $\sin \phi_L = 1$, and finite differences for the derivatives,

$$\frac{\omega_L^{n+1} - \omega_L^n}{\Delta t} = (E_L^n - C_L^n) - \frac{K}{R^2 (1 - \sin \phi_{L-1/2})} \cos \phi_{L-1/2} \frac{\omega_L^n - \omega_{L-1}^n}{\Delta \phi_L}. \quad (34)$$

Equations (30), (32) and (34) provide a complete set of discretized equations for the water content ω . Note that no boundary conditions at the poles are required, and no problems arise due to the singularity of Eq. (20) at the poles.

A.3 Instantaneous mixing

As mentioned at the end of Sect. 2.7, instantaneous mixing of water vapour in the atmosphere can be described as the limit of infinite diffusivity, $K \rightarrow \infty$. However, numerically, this limit cannot be carried out with the discretization described above. Instead, a two-step procedure needs to be applied for this case.

In the first step, for any point of the model domain ($l = 0, \dots, L$), let us compute predictors of the water content at the new time-step, $\hat{\omega}_l^{n+1}$, by ignoring the water transport,

$$\frac{\hat{\omega}_l^{n+1} - \omega_l^n}{\Delta t} = E_l^n - C_l^n. \quad (35)$$

In the second step, the resulting total amount of water shall be mixed over the entire planet. The total amount of water is obtained by integrating over the grid cells and summing up,

$$\begin{aligned} \omega_{\text{tot}} &= 2\pi R^2 \hat{\omega}_0^{n+1} \int_{\phi_0}^{\phi_{1/2}} \cos \phi \, d\phi + \sum_{l=1}^{L-1} 2\pi R^2 \hat{\omega}_l^{n+1} \int_{\phi_{l-1/2}}^{\phi_{l+1/2}} \cos \phi \, d\phi \\ &\quad + 2\pi R^2 \hat{\omega}_L^{n+1} \int_{\phi_{L-1/2}}^{\phi_L} \cos \phi \, d\phi \\ &= 2\pi R^2 \left\{ \hat{\omega}_0^{n+1} (1 + \sin \phi_{1/2}) + \sum_{l=1}^{L-1} \hat{\omega}_l^{n+1} (\sin \phi_{l+1/2} - \sin \phi_{l-1/2}) \right. \\ &\quad \left. + \hat{\omega}_L^{n+1} (1 - \sin \phi_{L-1/2}) \right\}. \end{aligned} \quad (36)$$

For all points $l = 0, \dots, L$, the new water content follows by division by the surface of the planet,

$$\omega_l^{n+1} = \frac{\omega_{\text{tot}}}{4\pi R^2} = \frac{1}{2} \left\{ \hat{\omega}_0^{n+1} (1 + \sin \phi_{1/2}) + \sum_{l=1}^{L-1} \hat{\omega}_l^{n+1} (\sin \phi_{l+1/2} - \sin \phi_{l-1/2}) \right. \\ \left. + \hat{\omega}_L^{n+1} (1 - \sin \phi_{L-1/2}) \right\}. \quad (37)$$

A.4 Ice evolution

The discretization of the ice-thickness equation (22) is straightforward. By using an Euler forward step for the time derivative, we obtain

$$\frac{H_l^{n+1} - H_l^n}{\Delta t} = (a_{\text{net}})_l^n = \frac{C_l^n - E_l^n}{\rho_{\text{ice}}}. \quad (38)$$